ACS APPLIED MATERIALS & INTERFACES

Research Article

www.acsami.org

Mechanisms of Enhanced Optical Absorption for Ultrathin Silicon Solar Microcells with an Integrated Nanostructured Backside Reflector

Christopher J. Corcoran,[†] Somi Kang,[§] Lanfang Li,[§] Xiaoying Guo,[†,§] Debashis Chanda,*[,∥] and Ralph G. Nuzzo*[,†,§]

[†]Department of Chemistry, University of Illinois at Urbana-Champaign, 505 South Matthews Avenue, Urbana, Illinois 61801, United States

[§]Department of Materials Science and Engineering, Frederick Seitz Materials Research Laboratory, University of Illinois at Urbana-Champaign, 1304 West Green Street, Urbana, Illinois 61801, United States

[∥]NanoScience Technology Center and College of Optics and Photonics (CREOL), University of Central Florida, 12424 Research Parkway Suite 400, Orlando, Florida 32826, United States

Supporting Information

ABSTRACT: This paper investigates mechanisms of enhanced light absorption exhibited by ultrathin Si solar microcells integrated with a periodically nanostructured, semitransparent metallic reflector. This backside reflector comprises periodic nanoscale relief features formed by soft-imprint lithography with a thin (~35 nm) coating of Au. The work shows that microcells placed in direct contact above the nanostructured reflector's surface creates Fabry–Pérot cavities, which traps impinging light inside the Si slab via the excitation of cavity modes. Experimental measurements show that the short-circuit current and efficiency values for devices incorporating this thin, semitransparent backside reflector outperform similar Si microcells integrated with a planar thick (~300 nm) opaque mirror by ~10–15% because of enhanced absorption. Computational modeling that is supported by experimental measurements reveal that the dominant methods of enhancement stem from a complex interplay between backside diffraction/scattering and Fabry–Pérot resonances. These same data demonstrate that plasmonic interactions contribute minimally to the optical enhancements seen.

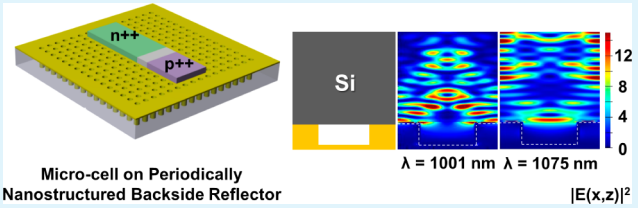

KEYWORDS: *light trapping, photovoltaics, optical nanostructures*

1. INTRODUCTION

Photovoltaic (PV) technologies are playing an increasingly important role in designs for current and future energy infrastructures. As an absorber material, silicon (Si), retains a dominant position in the terrestrial PV market because of its high natural abundance,[1] good optical properties,[2] and electronic properties,[3] along with its well-established production and processing methods.[4] Silicon-based devices are typically designed to be thick enough to enable full absorption of the solar photon flux up to the limits established by the material's band gap.[5] As a consequence, these optically-opaque devices can be expensive, bulky, and fragile. Engineering thin-film alternatives to conventional devices may reduce system costs as well as enable potentially more effective designs with new capabilities. An example of this comes from our previous work with large-scale arrays of ultrathin Si solar microcells fabricated from bulk wafers.[6] These devices demonstrated a high degree of mechanical flexibility and, therefore, improved durability that is unusual to Si. The drawback in reducing the thickness of the active material is that the absorption of photons can be reduced greatly, which reduces device performance. A thin-film cell, however, can perform as well as, or possibly better than, its thicker counterpart[7] if light trapping methods are employed to extend the path length and/or the light intensity is enhanced inside the semiconductor slab.

In recent reports, we have described methods for improved light trapping in thin-Si solar cells, including using nanostructured relief features on the surface of the device,[8] wherein absorption is increased through diffraction or scattering; three-dimensional photovoltaic device geometries that enable the capture of more photons;[9] and passive concentration by employing luminescent waveguides,[10] which offers the advantage of harvesting both direct and diffuse photons from the surrounding environment.

Several avenues have been investigated for enhancing the absorption of light in thin-film PV devices. Plasmonic optical designs is one active area of research that has attracted considerable attention, with the goal of increasing the

Received: January 31, 2013
Accepted: April 15, 2013
Published: April 15, 2013

absorption cross-section of the active layer by placing metallic sub-wavelength optical elements on the surface, inside, or on the backside of the solar cell.[5,11−16] It is demonstrated in this work that PV devices integrated with plasmonic components can yield increased photocurrents, with benefits evidenced in systems based on both inorganic and organic semiconductors. Another technique to increase light absorption via light-trapping involves harnessing whispering-gallery modes,[17,18] as well as textured surfaces.[19,20] These and other techniques of trapping light inside PV devices have been reviewed in depth in the literature.[11,21] Processes to integrate light-trapping/management structures in future generation PV technologies are of particular interest, with notable examples illustrating the varying facilities of optical integration at different stages of materials growth,[22,23]device fabrication,[13,24] and module integration.[17]

In this paper, we investigate and characterize design principles for integrated sub-visible wavelength optics that can be used to improve the key operating parameters of PV devices. We specifically examine an embossed "3D plasmonic crystal" from our earlier work[25,26] for use as a backside reflector that, when integrated with a Si microcell, yields performance gains greater than those observed with a conventional mirror. The complex interactions that occur between this periodically nanostructured reflector (PNR) and the Si microcell are examined in depth in this work. Our findings compliment and extend those of earlier work on periodically nanostructured metallic or dielectric-based backside reflectors integrated with thin-film amorphous, monocrystalline, and microcrystalline Si solar cells.[27−32] We specifically show that in addition to mechanisms addressed in previous reports, significant enhancements are evidenced that stem from Fabry−Pérot-cavity-type resonances created at the microcell−PNR interface. These cavities are formed when a microcell with a flat backsurface is placed in proximate contact with the PNR. These Fabry−Pérot cavities trap light as standing waves at specific (design-directed) resonant frequencies which in turn serves to enhance the photocurrent.[33] The cavity architecture formed by the compliant contact of the microcell and PNR distinguishes this system from the conformal material coatings, mainly of amorphous Si, used in earlier studies of PV designs incorporating periodically nanostructured and randomly textured backsurfaces,[13,21,24,29,30] which are complicated because of potential increases in carrier collection from an enlarged active area.[34] The current work also speaks to perplexing issues of the relative importance of design rules, as raised in a recent study showing minimal differences in performance enhancements between a periodically nanostructured reflector from a randomly textured one (despite computational modeling predicting the periodic texture to be superior).[29] The data and theoretical modeling results reported here highlight an important attribute of PNRs that strongly mediate their performance and further demonstrate that plasmonic enhancement mechanisms do not make a significant contribution to the enhancements seen. The enhanced cross sections that result from Fabry−Pérot-based mechanisms supported by the PNRs reported here appear to be quite general and we believe might beneficially be extended to a random distribution of cavities of various depths, pitches, and diameters so long as they can couple the light transmitted through Si to cavity modes at wavelengths not absorbed from the first pass through the microcell. We have not carried out steps to optimize the intrinsic performance of the thin microcells used as reported in these studies, adopting instead cells derived from an SOI-based fabrication protocol[9] because of the exceptional smoothness of the backside surface that is required for successful device assembly by an adhesive-free transfer printing protocol.[35−37]

The PNR, a metal-coated plasmonic crystal, consists of a semitransparent (thickness ∼35 nm) layer of gold (Au) conformally coating nanowell relief features embossed by soft-imprint lithography.[26] The experimental measurements discussed below show that Si microcells on the PNR have short-circuit current density (J_{sc}) values that exceed the values from the same microcells when placed above flat, opaque mirrors (thickness ∼300 nm) of the same metal by ∼10−15%, a striking observation given the semitransparent PNR can outperform a traditional thick opaque mirror. Finite-difference time domain (FDTD) simulations confirm that the main component of the enhanced absorption seen experimentally comes from 0th and higher diffraction order Fabry−Pérot resonances. To provide a more quantitative understanding of the mechanisms involved photocurrent measurements with microcells on the PNR are compared to measurements made with microcells above flat, opaque backside reflectors and flat reflectors with an identical semitransparent thickness of metal. Wavelength dependent measurements demonstrate that the observed enhancements occur at the computationally predicted wavelengths of light for cavity-mode-based mechanisms. Plasmonic influences were ruled out based upon studies using Al and Ag backside reflectors which suggest no contribution of surface plasmons to the enhancement in the photocurrent.

2. MATERIALS AND METHODS

2.1. Fabrication of the Si Microcells. The fabrication strategy utilizes silicon-on-insulator (SOI; p-type device layer 2 μm ± 0.5 μm; 10-20 ohm-cm; 1 μm thick box; 300 μm thick handle; Ultrasil) wafers in a manner similar to previously published devices.[9] An image outlining the fabrication of the microcells is presented in Supporting Information Figure S1. The p−n junction is formed by selective area diffusion of boron (p++) and phosphorous (n++) from solid doping sources (Saint-Gobain Ceramics). Plasma-enhance chemical vapor deposition (PECVD)-grade oxide (∼600 nm thick) is used as a doping mask for each diffusion step. Before each doping step the wafers are cleaned with the RCA-1/RCA-2 cleaning process at 70-80°C for ten minutes each. (RCA-1 = 1:1:5 $NH_4OH/H_2O_2/H_2O$ and RCA-2 = 1:1:5 $HCl/H_2O_2/H_2O$.) The conditions for doping are the following: 10 min exposure at 1000°C for phosphorous and 30 min exposure at 1000°C for boron. A photoresist mask (AZ 5214, Clariant) on the surface is applied to define the side-walls, anchors, and trenches of the microcells. Inductively coupled plasma reactive-ion etching (STS-ICPRIE, STS Mesc Multiplex Advanced Silicon Etcher) is used to etch these features and generate straight side-walls and corners.

The conditions for ICP-RIE have been reported previously.[38] The parameters are as follows: O_2/SF_6 = 13/130 sccm (for the silicon etching step) and C_4F_8= 110 sccm (for passivation); gas pressure: 94 mTorr, etching power: 600/12 W inductively coupled plasma (ICP)/platen (P), deposition power: 600/0 W for ICP/P, etching duration: 7 s, and deposition duration: 5 s. Thicknesses of the device layer were measured with a profilometer after etching in the ICP-RIE instrument.

To allow for easier retrieval of the microcells, the anchors are anisotropically etched in KOH (Fisher) at 75°C for one minute. This anisotropic etching step creates sharp-angled corners in order to facilitate stress focusing for controlled fracture.[39] A PECVD-grade oxynitride mask (∼100 nm) on the surface of the wafer serves as a passivation layer during KOH etching. The buried oxide layer is removed with 49% HF (Transene) and the microcells are suspended on the wafer by their anchors. (***Caution:*** *HF is a highly corrosive and toxic. Users should wear goggles, a lab coat, and natural rubber, neoprene, or Viton gloves when working with this chemical.*) It is also important to

cover the samples while submerged in concentrated HF to minimize porous silicon formation.[40] The sample is then placed briefly (~3 s) in KOH at 40°C to roughen the surface of the device as well as remove any porous silicon that may have generated during the HF etching step.

2.2. Fabrication of the Backside Reflectors. Fabrication of the PNR utilizes soft lithography and follows published procedures.[25,26,41] Briefly, large-area (5 × 5 mm^2) square arrays of subwavelength cylindrical depressions were molded onto the surface of a thin layer of a photo-curable epoxy (NOA 73, Norland), wherein a PDMS (10:1 Sylgard 184) mold containing the inverse pattern was pressed into the epoxy and cured under ultraviolet light. Blanket deposition of titania (~8 nm) for a thin adhesion layer and Au (~35 nm) by sputter coating at 5 mTorr completed the PNR. The features for all periodically arrayed reflectors reported herein have a relief depth of ~380 nm, a hole pitch of Λ~740 nm, and a hole diameter of ~440 nm, as verified by atomic force microscopy (not shown) and SEM measurements. A thin layer of alumina is then deposited on each backside reflector by atomic layer deposition (ALD; Cabridge Nanotech; sample temperature 80°C; trimethylaluminum/H_2O; 10 sccm N_2, 0.03 s pulse; 0 s exposure/pump valve close length; 65 s pump/length of time between pulses), which acts as a thin insulating layer to prevent direct Si to Au contacts. The thickness of the alumina was verified with an ellipsometer on a reference piece of Si.

Not having the insulator on the surface of each reflector was found to decrease J_{sc} values. (Supporting Information Figure S2 compares J_{sc} values for different materials used as an insulating layer.) The decrease in J_{sc} seen in the presence of configurations that involve direct Si−Au reflector contacts can be attributed to enhanced carrier recombination at the Si-metal interface. Si and Au have different work functions and when brought into contact their Fermi levels match at the interface, which results in metal-induced gap states. As these gap states occur deeper in the semiconductor than in the metal,[42] an unwanted bottom contact is created that hinders device performance.

This thickness of Au was chosen since it is almost optically opaque in the visible/NIR, where our Si microcells are optically transparent. The periodicity and structure of the PNR were chosen based on experimental measurements with microcells above PNRs with varying hole diameters and pitches. The structure with a pitch of Λ ≈ 740 nm and a hole diameter of ~440 nm was found to give the greatest enhancements in photocurrent (see Supporting Information Figure S3). Fabrication of Ag- and Al-PNRs and opaque mirrors followed similar ALD deposition and sputter-coating procedures.

2.3. FDTD Model. For the FDTD studies, a Drude plus two-pole Lorentzian model for the complex frequency-dependent Au permittivity was employed, with parameters fit to empirical dielectric constant data.[43] The structure was excited with linearly polarized, plane-wave light as described in ref 43. Here we used FDTD to "fit" our transmission data, shown in Supporting Information Figure S4, and then use that model, with those fitted parameters, to produce the absorption spectra. For the modeled spectra, the Au thickness parameters are 35 nm on the surface (determined through ellipsometry) and 12 and 20 nm on the sidewalls and bottoms of the relief features, respectively, as established by transmission electron microscopy measurements reported in a previous publication.[25] The PNR was modeled to have a relief depth of 380 nm, a hole pitch of Λ = 740 nm, and a hole diameter of 440 nm. Each backside reflector was modeled to have 10 nm of alumina above its surface with the 10 nm layer extending along the side walls and bottom of the relief features.

2.4. *J*−*V* Measurements. All current density-voltage (*J*−*V*) measurements reported below were made under air mass 1.5D illumination calibrated to 1000 W/m^2 (Oriel, Model 91192) at room temperature with a source meter (Keithley, model 2400) using a Si reference cell for calibration of the simulator (Newport-Oriel, model 91150 V). Measurements were performed on individual microcells transfer printed to glass slides, PNRs, and flat mirrors.

2.5. Solar Cell Measurements with Apertures. To accurately characterize these devices and minimize multiple reflections of light around the perimeter of the solar cells,[44] an anodized Al cover having an aperture area of 2 × 2 mm^2 was placed over each substrate with another anodized Al backplate placed below the substrate supporting the microcell (see Supporting Information Figure S5). All measurements reported are based on the area of the microcell. Sample variance in the *J*−*V* results was quite large for microcells from different wafer batches. Conversion efficiencies for microcells between different wafers, as measured on a glass slide with the anodized Al backplate, ranged from 1.2% to 1.6%, open-circuit voltage (V_{oc}) values ranged from 390 to 450 mV, fill factors varied from 55% to 65%, and J_{sc} values ranged from 4.6 to 6.0 mA/cm^2. To overcome sample variance, each microcell was first measured on a glass slide and then transfer-printed to the desired reflector where the measurement was then repeated. This allowed each *J*−*V* measurement incorporating a reflector to be normalized to the one made on the glass slide.

The 2 × 2 mm^2 aperture is quite large relative to the area of the microcell (~2.5 × 10^4 μm^2). Experiments were performed wherein microcells on glass were measured with small-area apertures. These small-area apertures had an aperture area of 70 × 520 μm^2 and these *J*−*V* results were compared to the 2 × 2 mm^2 aperture results to verify that internal reflections of light were in fact small contributors to the cell's response. We observed a ~5−10% overall decrease in the J_{sc} with the small-area aperture vs the 2 × 2 mm^2 (large-area) aperture. Excessive light scattering from the backside reflectors is considered to be extremely minor given the height of the microcells as well as band-pass filter measurements on microcells inside the small-area apertures when compared to the large-area aperture results (see Supporting Information Figure S6). Because the small-area apertures use Au, they correctly match any excessive light scattering seen from backside reflector measurements. Additionally, compared to the large-area aperture measurements, relatively modest enhancements in the photocurrent (~5−10%) were observed in the visible part of the spectrum with the J_{sc} falling off in the NIR. The decrease in the J_{sc} in the NIR can be attributed to small amounts of light scattering off of the anodized Al backplate when the microcell is first measured on the glass slide with the large-area aperture vs the small-area aperture. Any enhancements in photocurrent reported therefore come mainly from light that passes through the front of the device. Because ~1.7 μm thick Si absorbs all of the photons with wavelengths of ~500 nm or greater in energy,[2] absorption enhancements with backside reflectors reported here can come only from longer wavelength photons that were not absorbed after the initial pass through the device. This is discussed in greater detail in the sections that follow.

3. RESULTS AND DISCUSSION

Figure 1a presents a schematic illustration of an individual microcell above the nanostructured surface. The microcells measure 500 μm in length, 50 μm in width, and ~1.7 μm in thicknesses and were fabricated from SOI wafers. Figure 1b shows a sparse array of microcells transfer printed to the surface of the PNR with their doping areas outlined in purple (p++) and green (n++). This doping profile places the p-n junction on the top of the microcell. The spacing between the p++ and n++ regions on the surface is 50 μm. This spacing provides a high internal electrical field to efficiently separate photogenerated electron−hole pairs.

To achieve direct contact onto the surface of each backside reflector, the microcells are transfer-printed without an adhesive layer. Adhesive-free transfer printing relies on the kinetic control of adhesion between a microcell and a polydimethylsiloxane (PDMS) stamp, where a slow peeling velocity favors adhesion between the microcell and backside reflector and a faster one favors adhesion between the microcell and PDMS stamp. The mechanics involved with transfer printing have been explored in other papers.[35−37] Working with SOI improves transfer printing results since the back surfaces of the microcells are extremely smooth, much more so than results from fabrication schemes used to fabricate microcells using bulk Si wafers. The etching processes used in these cases[6,38]

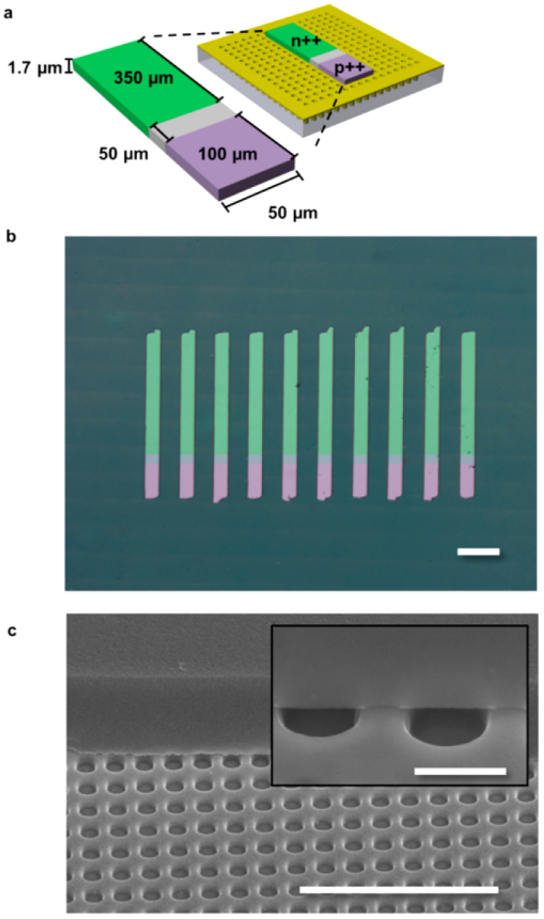

Figure 1. Schematic illustration, optical and SEM images of microcells. (a) Illustration of the solar microcell on the surface of the PNR (right) with an enlarged image giving the dimensions of the microcell (left). (b) Images of microcells transferred to the PNR with their doping profiles highlighted in green (n++) and purple (p++). (c) SEM image of a microcell transfer printed to the PNR with the inset showing direct contact of the microcell to the surface of the PNR. White lines in parts (b and c) represents: 100 μm (b); 5 μm (c); and 500 nm (c, insert).

generates a back surface too rough for standard forms of adhesive-free transfer printing. A scanning electron microscope (SEM) image of a microcell transfer printed to an Au-coated PNR is presented in Figure 1c; the inset shows a zoomed-in profile for the Si-PNR interface which demonstrates the direct contact at the backsurface between the reflector and microcell to form the Fabry-Pérot-cavities.

Figure 2a depicts the simulated optical absorption for 1.7 μm thick bare Si without any reflector (black), above a 300 nm thick Au mirror (blue), and above the PNR (red). For Si without any backside reflector, the absorption is poor; it absorbs less than 60% of the light at 600 nm and light absorption quickly diminishes further into the NIR region of the spectrum. The peaks seen in all the plots given in the figure can be attributed to Fabry−Pérot resonances. To understand the detailed nature of these resonances we performed 3D FDTD simulations. Fig. 2b presents FDTD-computed, cross-sectional electric field distributions ($|E(x,z)|^2$) at various wavelengths for both reflectors. The illustrations to the far left of Figure 2b are a depiction of each modeled system. As is evident from the data given in Figure 2b, at $\lambda \approx 675$ nm (point 1 on Figure 2a) the absorption for both backside reflectors (opaque and PNR) is characteristic of 0th-order Fabry−Pérot resonances, which occur at the same positions as on spectra of Si without a backside reflector (Figure 2a). The absorption peak at $\lambda \approx 675$ nm for the Au mirror is marginally stronger than the absorption peak corresponding to the PNR because of total back reflection from the opaque mirror. The same trend persists where Si on the opaque Au mirror absorbs more light than the Si on the Au PNR up to 800 nm. After 800 nm the absorption peaks for Si on the mirror quickly diminish and the PNR case begins to outperform all the way through the NIR part of the spectrum. In the NIR domain, there appear to be intense, broadened peaks in the absorption plot for the Si above the PNR due to the presence of strong steep angle 1st-order Fabry−Pérot resonances (other higher (> 1) diffraction orders are negligible because of the combination of the period and the excitation wavelengths) as evident in the cross-sectional images of Figure 2b for λ = 1001 and 1075 nm; these two wavelengths clearly show 1st-order standing wave interference patterns. This effect is pronounced for the longer wavelength range as the first order angle varies as $\theta_1 = \sin^{-1}[\lambda/n(\lambda)\Lambda]$, and consequently the path length increases with λ; we also identified these Fabry−Pérot resoances as 0th- and 1st-order cavity modes through an effective medium calculation. Additional wavelength dependent cross-sectional images are provided in Supporting Information Figure S7.

Figure 3a depicts the enhancement in J_{sc} for each reflector as a function of insulating layer thickness. The amount of alumina was varied to find the thickness that optimized electrical insulation between Au and the microcell, which was determined to be between 5−10 nm. At 10 nm of alumina on each reflector, Figure 3a shows a ∼15% enhancement in the photocurrent when the microcell is on the surface of the flat, opaque reflector while there is a ∼26% enhancement in the photocurrent when the microcell is on the PNR. We also performed measurements with a 35 nm thick, flat Au BSR and found the enhancement in the J_{sc} to be ∼10% relative to the anodized Al backplate. The measured J_{sc} remains constant as the amount of alumina on the Au mirror is increased. A different result is observed for thicker layers of alumina on the PNR. The PNR has an observed drop in enhancement going beyond 10 nm of alumina. (See Figure S8 in the Supporting Information for a comparison in FDTD-computed absorption spectra for Si on a PNR with 10 nm of alumina versus 40 nm of alumina.) From the FDTD computations, we found that the electric field enhancements extend ten nanometers at the edges of the Au nanowells (because of localized surface plasmons) to hundreds of nanometers and all way through the Si slab (corresponding to 0th and higher diffraction order Fabry−Pérot resonances). Figure 3a shows that 20 nm of alumina has an enhancement slightly higher than the Au mirror. Figure 3b shows representative $J-V$ measurements for microcells prepared on glass (black), above the Au mirror (blue), and above the Au PNR (red) and Table 1 gives their key parameters. The microcell on glass has an initial efficiency of 1.40% with FF = 61%, V_{oc} = 410 mV, and J_{sc} = 5.61 mA/cm^2. Once transferred to the PNR, Eff = 1.75%, FF = 60%, V_{oc} = 419 mV, and J_{sc} = 7.02 mA/cm^2. A similar performing microcell was transferred to an Au mirror and had the following characteristics: Eff = 1.59%, FF = 60%, V_{oc} = 417 mV, and J_{sc} = 6.42 mA/cm^2. The slight enhancement in the V_{oc} (relative to the microcell on the glass slide) is to be expected since V_{oc} increases logarithmically with illumination intensity.[45] For the present case we measured almost the same FFs for representative cells above the Au PNR

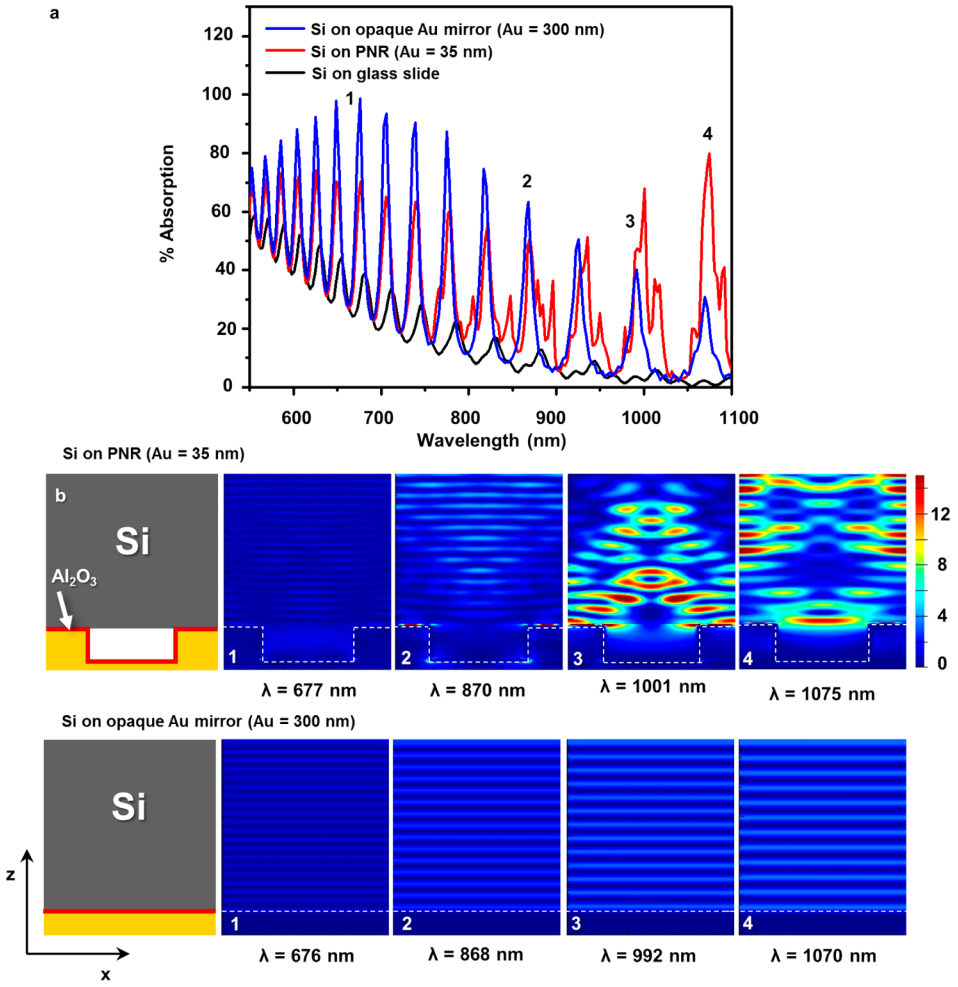

Figure 2. FDTD absorption and cross-section images of microcells. (a) FDTD plot depicting the absorption for 1.7 μm thick Si microcell (black), on a 300 nm thick, flat Au backside reflector (blue), and the PNR (red). (b) Illustrations of each modeled system along with cross-sectional (X–Z) images computed with FDTD of the electric field distribution of one unit cell for a microcell on the surface of the PNR (top) and the flat, Au backside reflector (bottom). The simulations were performed with 10 nm of Al_2O_3 (outlined in red in each illustration) between each backside reflector and the microcell. The white region for the PNR case (b) represents an air-gap between the Si microcell and the PNR interface. The PNR was modeled to have a relief depth of 380 nm, a hole pitch of Λ = 740 nm, and a hole diameter of 440 nm. Images are shown for wavelengths around 676 (point 1), 870 (point 2), 1000 (point 3), and 1070 nm (point 4).

and the Au mirror, indicating negligible changes in the series resistance. We also found that slightly higher efficiencies occur in the PNR case because of the enhanced absorption induced by Fabry–Perot resonances. Because of the large surface-area-to-volume ratio of these microcells, as well as the fact that these devices have no passivation layer (a choice made to simplify the fabrication of thin microcells with the extremely flat back surfaces, as required for adhesive free transfer printing, from the SOI source wafer), carrier recombination at the surface is quite high (as shown by the low V_{oc} values).

We should note that these SOI-derived microcells, although functional, are of relatively low performance as compared to both commercial Si solar cells and microcells we have previously reported.[6,8,10] Their use serves solely to facilitate a proof-of-concept on the qualities realized by the precise placement of a PNR in proximate planar contact with the cell. The lower performance of these devices is a well-understood result of the fabrication process,[9] which is not optimized. The performance is affected by the lack of a surface passivation layer encapsulating the microcells as well as the microcells not possessing a back-surface field.[46,47] Additional factors that impact our cell performance include the lack of an anti-reflective coating,[46,47] a highly doped emitter, and having top and bottom surfaces that are nearly atomically flat, which reduces the potential for multiple internal reflections of light. Work is currently in progress that is developing improved fabrication methods and integration schemes for ultrathin cells that mitigate many of these impacts.

Photocurrent measurements based on a given wavelength range, up to the material's bandgap as measured using filters placed in front of the solar simulator, are given in Figure 3c. The graph is plotted in terms of enhancement factor where measurements for microcells on the PNR are normalized to measurements for microcells on the flat, opaque Au backside reflector (red) with accompanying FDTD results for the Si slab above the PNR normalized to the Si slab above the flat, opaque Au (blue). The horizontal error bars depict the wavelength range measured while the vertical error bars represent measured sample variance. To study the wavelength dependent absorption enhancement, band pass filters were used to measure absorption for specific wavelength ranges. The band-pass filters had the following center wavelengths: 550 (FWHM

dx.doi.org/10.1021/am400408g | ACS Appl. Mater. Interfaces 2013, 5, 4239–4246

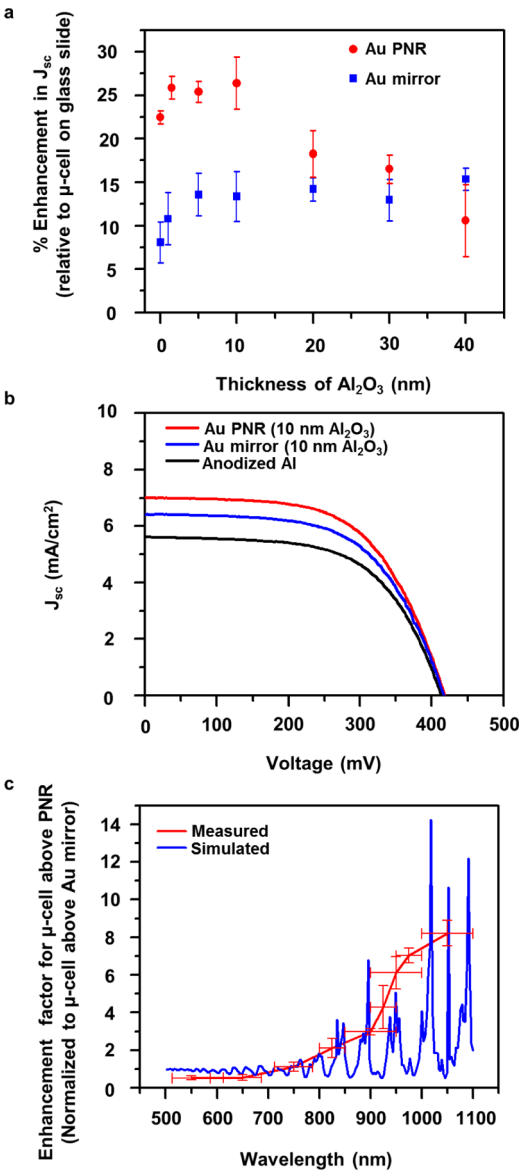

Figure 3. $J-V$ measurements of microcells under illumination. (a) Enhancements in the J_{sc} for microcells on the PNR and flat, Au backside reflector as a function Al_2O_3 spacer layer thickness. Each backside reflector measurement has been normalized to the measurement of the microcell on a glass slide. (b) Representative $J-V$ measurements for microcells on a glass slide (black), PNR (red), and flat Au (blue) with a table giving the important cell parameters. (c) Enhancement factors for filter measurements performed under the solar simulator for microcells on the PNR normalized to microcells on the flat, opaque Au backside reflector (red) with accompanying FDTD results for the Si slab above the PNR normalized to Si slab above the flat, opaque Au (blue). *X*-axis error bars indicate the wavelength range for the filters while the *y*-axis error bars indicate sample variance.

Table 1. Cell Performance as a Function of Backside Reflector

backside reflector	Eff (%)	V_{oc} (mV)	J_{sc} (mA/cm^2)	FF (%)
Au PNR	1.75	419	7.02	60
Au Mirror	1.59	417	6.42	60
Anodized Al backplate	1.40	410	5.61	61

± 37.5 nm), 650 (FWHM ± 37.5 nm), and 750 nm (FWHM ± 37.5 nm). A combination of short-pass and long-pass filters had the following center wavelengths 825 (FWHM ± 25 nm), 900 (FWHM ± 50 nm), 925 (FWHM ± 25 nm), 950 (FWHM ± 50 nm), 975 (FWHM ± 25 nm), and 1050 nm (FWHM ± 50 nm). Similar to the FDTD results, the Au mirror marginally outperforms the PNR up until about 800 nm. After 800 nm the PNR outperforms the opaque backside reflector. The regions for absorption enhancement from the experimental data in Figure 3c agree quite well with the FDTD models given in Figure 2a. Photocurrent enhancements after 900 nm are the most drastic with the PNR having an enhancement factor ∼8 in the NIR.

A few of the cross-sectional images in Figure 2b show surface plasmons on the sides of the upper and lower portions of the Au nanowells. To rule out any contribution to the enhancement in the photocurrent from surface plasmons, filter measurements were also performed on microcells above Al- and Ag-based PNRs and their respective flat mirrors (see Supporting Information Figure S9). Ag and Al were studied since Au generates plasmons in the visible, Ag generates plasmons in the visible/NIR, and Al generates plasmons in the ultraviolet.[48−50] The benefit of studying the Al-based system is that no plasmons will be generated since Si absorbs and reflects all the ultraviolet light (where Al is active). The enhancement in the J_{sc} for each PNR and mirror were similar to their Au counterparts ∼26% and ∼15%, respectively, when compared to the anodized Al backplate. From the filter measurements, a similar trend was observed with the opaque mirror outperforming each metallic PNR in the shorter wavelength range. After 800 nm the PNR outperforms the mirror of the same metal as shown in Supporting Information Figure S9. Furthermore, the trends in J_{sc} for each reflector were similar to the reported reflection measurements of each backside reflector (Supporting Information Figure S10). These measurements therefore rule out dominating contributions from surface plasmons to the enhancements seen in the photocurrent. For the present PNR design, we haven't observed any important contributions from plasmonic effects over the silicon absorption bandwidth.

4. CONCLUSIONS

To summarize, we report on a semitransparent backside reflector with nanoscale relief features that can outperform an optically opaque, flat reflector of the same metal due to excitation of higher-order Fabry−Pérot resonances, as well as light diffraction/scattering. Si is an efficient absorber in the 400−700 nm wavelength range. The key objective of the PNR is to enhance absorption in the 750−1100 nm band. The photocurrent values for microcells above the PNR are ∼11% greater than for microcells above the opaque mirror and ∼26% greater than microcells without a reflector. We have identified the mechanisms that enable enhanced absorption for microcells above the PNR, as well as above the mirror. Computational modeling reveals that the major component for the increased absorption stems from higher-order Fabry−Pérot resonances. $J-V$ measurements incorporating filters below the solar simulator show higher photocurrent densities in the red/NIR domain of the spectrum, which agree with our computational model. These experimental results on working devices further support the notion that Fabry−Pérot resonances are the dominant mechanism for the enhanced photocurrent. Filter measurements with Al- and Ag-based PNRs and mirrors show similar trends in the J_{sc} to Au PNRs and mirrors and therefore rule out any possible contribution from surface plasmons to the

enhanced absorption. Solar cells utilizing back contacts, such as point-contact solar cells,[51−53] can benefit from the design principles and light management schemes established by this work. The key aspect to enable increased performance occurs when the device is in direct contact with the backside reflector. This allows the device to take advantage of the intense, near-field phenomena that enable a higher absorption cross-section and, therefore, better performance.

■ ASSOCIATED CONTENT

Supporting Information

Additional experimental and FDTD-modeled spectra, electric field cross-sectional images, J_{sc} comparisons of various dielectrics, small aperture measurements, and J_{sc} data of the various backside reflectors is available in the supporting information. This information is available free of charge via the Internet at http://pubs.acs.org/.

■ AUTHOR INFORMATION

Corresponding Author

*E-mail: r-nuzzo@illinois.edu (R.G.N.); debashis.chanda@creol.ucf.edu (D.C.).

Notes

The authors declare no competing financial interest.

■ ACKNOWLEDGMENTS

This work was financially supported by the Department of Energy through Energy Frontier Research Center under award number DE-SC0001293 (subcontract no. 67N-1087758). C.J.C. thanks A.-P. Le, H.-J. Chung, M. R. Hansen, G. A. Mensing, and A. A. Rockett for useful discussions; M. W. Cason and E. Brueckner for assistance with SEM images and solar cell illustrations; J. A. Rogers for computational resources to perform the FDTD simulations; P. V. Braun for use of his optical microscope; and the faculty and staff at the Materials Research Center, Micro- and Nanotechnology Laboratory, and the Micro-Nano-Mechanical Systems Cleanroom.

■ REFERENCES

(1) Ceccaroli, B.; Lohne, O. *Handbook of Photovoltaic Science and Engineering*, 2nd ed.; Luque, A., Hegedus, S., Eds.; John Wiley & Sons: West Sussex, U.K., 2011; p 169.
(2) Green, M. A.; Keevers, M. J. *Prog. Photovoltaics* **1995**, *3*, 189.
(3) Jacoboni, C.; Canali, C.; Ottaviani, G.; Quaranta, A. A. *Solid-State Electron.* **1977**, *20*, 77.
(4) Bagnall, D. M.; Boreland, M. *Energy Policy* **2008**, *36*, 4390.
(5) Atwater, H. A.; Polman, A. *Nat. Mater.* **2010**, *9*, 865.
(6) Yoon, J.; Baca, A. J.; Park, S.-I.; Elvikis, P.; Geddes, J. B.; Li, L.; Kim, R. H.; Xiao, J.; Wang, S.; Kim, T.-H.; Motala, M. J.; Ahn, B. Y.; Duoss, E. B.; Lewis, J. A.; Nuzzo, R. G.; Ferreira, P. M.; Huang, Y.; Rockett, A.; Rogers, J. A. *Nat. Mater.* **2008**, *7*, 907.
(7) Yablonovitch, E.; Cody, G. D. *IEEE Trans. Electron Devices* **1982**, *29*, 300.
(8) Shir, D.; Yoon, J.; Chanda, D.; Ryu, J. H.; Rogers, J. A. *Nano Lett.* **2010**, *10*, 3041.
(9) Guo, X. Y.; Li, H.; Ahn, B. Y.; Duoss, E. B.; Hsia, K. J.; Lewis, J. A.; Nuzzo, R. G. *Proc. Natl. Acad. Sci. U. S. A.* **2009**, *106*, 20149.
(10) Yoon, J.; Li, L. F.; Semichaevsky, A. V.; Ryu, J. H.; Johnson, H. T.; Nuzzo, R. G.; Rogers, J. A. *Nat. Commun.* **2011**, *2*, 343.
(11) Ferry, V. E.; Munday, J. N.; Atwater, H. A. *Adv. Mater.* **2010**, *22*, 4794.
(12) Ferry, V. E.; Sweatlock, L. A.; Pacifici, D.; Atwater, H. A. *Nano Lett.* **2008**, *8*, 4391.
(13) Ferry, V. E.; Verschuuren, M. A.; van Lare, M. C.; Schropp, R. E. I.; Atwater, H. A.; Polman, A. *Nano Lett.* **2011**, *11*, 4239.
(14) Pillai, S.; Beck, F. J.; Catchpole, K. R.; Ouyang, Z.; Green, M. A. *J. Appl. Phys.* **2011**, *109*, No. 073105.
(15) Pillai, S.; Green, M. A. *Sol. Energy Mater. Sol. Cells* **2010**, *94*, 1481.
(16) Wang, C. C. D.; Choy, W. C. H.; Duan, C. H.; Fung, D. D. S.; Sha, W. E. I.; Xie, F. X.; Huang, F.; Cao, Y. *J. Mater. Chem.* **2012**, *22*, 1206.
(17) Grandidier, J.; Callahan, D. M.; Munday, J. N.; Atwater, H. A. *Adv. Mater.* **2011**, *23*, 1272.
(18) Yao, Y.; Yao, J.; Narasimhan, V. K.; Ruan, Z. C.; Xie, C.; Fan, S. H.; Cui, Y. *Nat. Commun.* **2012**, *3*, No. 664, DOI: 10.1038/ncomms1664.
(19) Han, S. E.; Chen, G. *Nano Lett.* **2010**, *10*, 4692.
(20) Mavrokefalos, A.; Han, S. E.; Yerci, S.; Branham, M. S.; Chen, G. *Nano Lett.* **2012**, *12*, 2792.
(21) Jeong, S.; Wang, S.; Cui, Y. *J. Vac. Sci. Technol., A* **2012**, *30*, 060801.
(22) Kelzenberg, M. D.; Boettcher, S. W.; Petykiewicz, J. A.; Turner-Evans, D. B.; Putnam, M. C.; Warren, E. L.; Spurgeon, J. M.; Briggs, R. M.; Lewis, N. S.; Atwater, H. A. *Nat. Mater.* **2010**, *9*, 239.
(23) Garnett, E.; Yang, P. *Nano Lett.* **2010**, *10*, 1082.
(24) Ferry, V. E.; Verschuuren, M. A.; Li, H. B. T.; Verhagen, E.; Walters, R. J.; Schropp, R. E. I.; Atwater, H. A.; Polman, A. *Opt. Express* **2010**, *18*, A237.
(25) Maria, J.; Truong, T. T.; Yao, J. M.; Lee, T. W.; Nuzzo, R. G.; Leyffer, S.; Gray, S. K.; Rogers, J. A. *J. Phys. Chem. C* **2009**, *113*, 10493.
(26) Yao, J. M.; Le, A. P.; Gray, S. K.; Moore, J. S.; Rogers, J. A.; Nuzzo, R. G. *Adv. Mater.* **2010**, *22*, 1102.
(27) Zeng, L.; Yi, Y.; Hong, C.; Liu, J.; Feng, N.; Duan, X.; Kimerling, L. C.; Alamariu, B. A. *Appl. Phys. Lett.* **2006**, *89*, No. 111111, DOI: 10.1063/1.2349845.
(28) Sheng, X.; Liu, J. F.; Kozinsky, I.; Agarwal, A. M.; Michel, J.; Kimerling, L. C. *Adv. Mater.* **2011**, *23*, 843.
(29) Battaglia, C.; Hsu, C. M.; Soderstrom, K.; Escarre, J.; Haug, F. J.; Charriere, M.; Boccard, M.; Despeisse, M.; Alexander, D. T. L.; Cantoni, M.; Cui, Y.; Ballif, C. *ACS Nano* **2012**, *6*, 2790.
(30) Hsu, C. M.; Battaglia, C.; Pahud, C.; Ruan, Z. C.; Haug, F. J.; Fan, S. H.; Ballif, C.; Cui, Y. *Adv. Energy Mater.* **2012**, *2*, 628.
(31) Curtin, B.; Biswas, R.; Dalal, V. *Appl. Phys. Lett.* 2009, *95*.
(32) Zeng, L.; Bermel, P.; Yi, Y.; Alamariu, B. A.; Broderick, K. A.; Liu, J.; Hong, C.; Duan, X.; Joannopoulos, J.; Kimerling, L. C. *Appl. Phys. Lett.* **2008**, *93*, No. 231102, DOI: 10.1063/1.3269593.
(33) Hecht, E. *Optics*, 4th ed.; Addison Wesley: San Francisco, CA, 2002.
(34) Fung, D. D. S.; Qiao, L.; Choy, W. C. H.; Wang, C.; Sha, W. E. I.; Xie, F.; He, S. *J. Mater. Chem.* **2011**, *21*, 16349.
(35) Feng, X.; Meitl, M. A.; Bowen, A. M.; Huang, Y.; Nuzzo, R. G.; Rogers, J. A. *Langmuir* **2007**, *23*, 12555.
(36) Kim, S.; Wu, J. A.; Carlson, A.; Jin, S. H.; Kovalsky, A.; Glass, P.; Liu, Z. J.; Ahmed, N.; Elgan, S. L.; Chen, W. Q.; Ferreira, P. M.; Sitti, M.; Huang, Y. G.; Rogers, J. A. *Proc. Natl. Acad. Sci. U. S. A.* **2010**, *107*, 17095.
(37) Meitl, M. A.; Zhu, Z. T.; Kumar, V.; Lee, K. J.; Feng, X.; Huang, Y. Y.; Adesida, I.; Nuzzo, R. G.; Rogers, J. A. *Nat. Mater.* **2006**, *5*, 33.
(38) Baca, A. J.; Meitl, M. A.; Ko, H. C.; Mack, S.; Kim, H. S.; Dong, J. Y.; Ferreira, P. M.; Rogers, J. A. *Adv. Funct. Mater.* **2007**, *17*, 3051.
(39) Meitl, M. A.; Feng, X.; Dong, J. Y.; Menard, E.; Ferreira, P. M.; Huang, Y. G.; Rogers, J. A. *Appl. Phys. Lett.* **2007**, *90*, 083110.
(40) Korotcenkov, G.; Cho, B. K. *Crit. Rev. Solid State Mater. Sci.* **2010**, *35*, 153.
(41) Yao, J. M.; Stewart, M. E.; Maria, J.; Lee, T. W.; Gray, S. K.; Rogers, J. A.; Nuzzo, R. G. *Angew. Chem., Int. Ed.* **2008**, *47*, 5013.
(42) Rockett, A. *The Materials Science of Semiconductors*; Springer: New York, 2008.
(43) Gary, S. K.; Kupka, T. *Phys. Rev. B* **2003**, *68*, 045415.
(44) Emery, K. *Handbook of Photovoltaic Science and Engineering*, 2nd ed.; Luque, A., Hegedus, S., Eds.; John Wiley & Sons: West Sussex, U.K., 2011; p 797.

(45) Nelson, J. *Physics of Solar Cells*; Imperial College Press: London, 2003.
(46) Green, M. A. *Semicond. Sci. Technol.* **1993**, *8*, 1.
(47) Wenham, S. R.; Green, M. A. *Prog. Photovoltaics* **1996**, *4*, 3.
(48) Mulvaney, P. *Langmuir* **1996**, *12*, 788.
(49) Link, S.; El-Sayed, M. A. *J. Phys. Chem. B* **1999**, *103*, 8410.
(50) Gao, H. W.; Henzie, J.; Lee, M. H.; Odom, T. W. *Proc. Natl. Acad. Sci. U. S. A.* **2008**, *105*, 20146.
(51) Suwito, D.; Jager, U.; Benick, J.; Janz, S.; Hermle, M.; Glunz, S. W. *IEEE Trans. Electron Devices* **2010**, *57*, 2032.
(52) Ok, Y. W.; Kang, M. G.; Kim, D.; Lee, J. C.; Yoon, K. H. *Curr. Appl. Phys.* **2009**, *9*, 1186.
(53) Swanson, R. M.; Beckwith, S. K.; Crane, R. A.; Eades, W. D.; Kwark, Y. H.; Sinton, R. A.; Swirhun, S. E. *IEEE Trans. Electron Devices* **1984**, *31*, 661.